

Ligand-assisted cation-exchange engineering for high-efficiency colloidal $\text{Cs}_{1-x}\text{FA}_x\text{PbI}_3$ quantum dot solar cells with reduced phase segregation

Mengmeng Hao¹, Yang Bai^{1*}, Stefan Zeiske², Long Ren³, Junxian Liu⁴, Yongbo Yuan⁵, Nasim Zarrabi², Ningyan Cheng³, Mehri Ghasemi¹, Peng Chen¹, Miaoqiang Lyu¹, Dongxu He¹, Jung-Ho Yun¹, Yi Du¹, Yun Wang¹, Shanshan Ding¹, Ardalan Armin², Paul Meredith², Gang Liu¹, Hui-Ming Cheng^{1,6,8,9} and Lianzhou Wang^{1*}

The mixed caesium and formamidinium lead triiodide perovskite system ($\text{Cs}_{1-x}\text{FA}_x\text{PbI}_3$) in the form of quantum dots (QDs) offers a pathway towards stable perovskite-based photovoltaics and optoelectronics. However, it remains challenging to synthesize such multinary QDs with desirable properties for high-performance QD solar cells (QDSCs). Here we report an effective oleic acid (OA) ligand-assisted cation-exchange strategy that allows controllable synthesis of $\text{Cs}_{1-x}\text{FA}_x\text{PbI}_3$ QDs across the whole composition range ($x=0\text{--}1$), which is inaccessible in large-grain polycrystalline thin films. In an OA-rich environment, the cross-exchange of cations is facilitated, enabling rapid formation of $\text{Cs}_{1-x}\text{FA}_x\text{PbI}_3$ QDs with reduced defect density. The hero $\text{Cs}_{0.5}\text{FA}_{0.5}\text{PbI}_3$ QDSC achieves a certified record power conversion efficiency (PCE) of 16.6% with negligible hysteresis. We further demonstrate that the QD devices exhibit substantially enhanced photostability compared with their thin-film counterparts because of suppressed phase segregation, and they retain 94% of the original PCE under continuous 1-sun illumination for 600 h.

Solution-processed organic–inorganic lead halide perovskite materials with a common formulation of ABX_3 (where A is an organic cation or Cs; B is commonly Pb or Sn; X is a halide) have shown promise in many applications, including photovoltaics (PVs)^{1–4}, light-emitting diodes (LEDs)^{5,6} and lasers^{7,8}. This potential is in part due to a range of desirable optoelectronic properties, such as large absorption coefficient, long carrier diffusion length and low exciton dissociation energy. The rapidly increasing power conversion efficiencies (PCEs) for perovskite solar cells (PSCs), which have been achieved with mixed methylammonium (MA) and formamidinium (FA) A-site cations and mixed Br and I X-site anions, have matched or surpassed other more established technologies, such as multicrystalline silicon, cadmium telluride and copper indium gallium selenide photovoltaics^{9–11}. However, device degradation due to MA degassing and photoinduced halide segregation remains a critical hurdle for commercialization^{12–14}. $\text{Cs}_{1-x}\text{FA}_x\text{PbI}_3$ without Br and volatile MA was recently demonstrated as a promising perovskite formulation, showing enhanced moisture-, thermal- and photostability^{12–14}. Unfortunately, solar cells using $\text{Cs}_{1-x}\text{FA}_x\text{PbI}_3$ perovskites suffer from large open circuit voltage (V_{OC}) losses, despite rubidium or polymer passivation^{12,14,15}, and thus their PCEs still lag behind those of the state-of-the-art perovskites containing MA and Br. Furthermore, it is still challenging to continuously tune the compositions of $\text{Cs}_x\text{FA}_{1-x}\text{PbI}_3$ at room temperature¹⁶, and

a high percentage ($x \geq 0.15$) of Cs incorporation can cause cation segregation under continuous illumination or with an applied bias^{13,17}. This hinders optical bandgap optimization and long-term operational stability for tandem solar cells and colour tuning of LEDs^{13,18,19}.

A promising approach towards mitigation of these challenges lies in the synthesis of perovskites in the form of nanometre-sized quantum dots (QDs) or nanocrystals. Perovskite QDs have shown notable advantages over their large-grain perovskite thin-film (often called bulk) counterparts. These advantages include additional bandgap tuning by utilizing the quantum-confinement effect²⁰, multiexciton generation²¹, near-unity photoluminescence quantum yield (PLQY)^{20,22} and photon up- and down-conversion^{23,24}. Thus, QDs offer great promise to surpass the Shockley–Queisser limit²⁵ and further boost the efficiency of tandem devices. Another advantage of perovskite QDs is the colloidal synthesis and industrially compatible processing at room temperature, which enables more convenient manufacturing by decoupling grain crystallization from film deposition²⁶. More importantly, both colloidal CsPbI_3 and FAPbI_3 QDs exhibit significantly enhanced phase stability at room temperature^{26,27} in comparison with their bulk counterparts, providing a strategy for improving the lifetime of PSCs. Perovskite QDs that are defect-tolerant have shown great promise over traditional chalcogenide QDs when incorporated into PV devices²⁰. CsPbI_3

¹Nanomaterials Centre, Australian Institute for Bioengineering and Nanotechnology and School of Chemical Engineering, The University of Queensland, St Lucia, Queensland, Australia. ²Department of Physics, Swansea University, Swansea, UK. ³Institute for Superconducting and Electronic Materials, Australian Institute for Innovative Materials, University of Wollongong, Wollongong, New South Wales, Australia. ⁴School of Environment and Science, Centre for Clean Environment and Energy, Griffith University, Gold Coast, Queensland, Australia. ⁵Institute of Super-Microstructure and Ultrafast Process in Advanced Materials, School of Physics and Electronics, Central South University, Changsha, China. ⁶Shenyang National Laboratory for Materials Science, Institute of Metal Research, Chinese Academy of Sciences, Shenyang, China. ⁷School of Materials Science and Engineering, University of Science and Technology of China, Shenyang, China. ⁸Shenzhen Geim Graphene Center, Tsinghua-Berkeley Shenzhen Institute, Tsinghua University, Shenzhen, China. ⁹Advanced Technology Institute, University of Surrey, Guildford, UK. *e-mail: y.bai@uq.edu.au; l.wang@uq.edu.au

QD solar cells (QDSC) have delivered a larger V_{OC} ^{26,28} than their thin-film counterparts, yielding a certified PCE of 13.4% (ref. ²⁹), which breaks the record for efficiency of PbS QDSCs. However, both CsPbI₃ and FAPbI₃ QDs are highly susceptible to moisture and polar solvents during postsynthesis purification and surface treatment^{26,27,30,31}. This poses challenges in effective ligand engineering and causes a significant increase in surface defects, which limits the carrier transport and thus the PCE enhancement.

Mixed-cation Cs_{1-x}FA_xPbI₃ QDs are more desirable than pure CsPbI₃ and FAPbI₃ QDs in terms of stability and charge transport properties. This is because the concomitant incorporation of FA and Cs induces entropic stabilization of the perovskite structure under ambient conditions¹⁶, and the fast rotation of FA results in enhanced orbital overlap and easier polaron formation, which leads to longer carrier lifetimes and reduced non-radiative recombination^{32,33}. Unfortunately, the rational synthesis of such multinary QDs with desirable optoelectronic properties remains a challenge as it is governed by a number of factors, such as the thermodynamics of the mixed-cation phases, crystal surface energies, ligand-binding dynamics and chemical equilibria in precursor solutions^{34,35}. Hence, only a few studies have been reported so far (for example, droplet-based microfluidics, cation exchange) that explore the synthesis of Cs_{1-x}FA_xPbI₃ QDs^{34–37}, but, in these cases, their use as a single light-absorbing layer in QDSCs resulted in deteriorated PCEs³⁶ and thus the PCEs of state-of-the-art QDSCs³⁸ still lag far behind those of their thin-film counterparts.

Here, we report a ligand-assisted cation-exchange strategy to synthesize high-quality Cs_{1-x}FA_xPbI₃ QDs in a time-efficient manner. We show that the surface ligands are important for the formation and diffusion of A-site cation vacancies, which play a critical role in driving the cross-exchange of cations. Compared with pure CsPbI₃ or FAPbI₃ QDs, the resultant Cs_{1-x}FA_xPbI₃ QDs are far more stable in ambient air or polar solvents and exhibit significantly lower trap density and longer carrier lifetimes. Solar cells fabricated with colloidal Cs_{0.5}FA_{0.5}PbI₃ QDs under ambient conditions deliver a certified steady-state PCE of 16.6%, outperforming other QDSC technologies¹¹. We also observe a larger PLQY of 10% and thus reduced non-radiative recombination in perovskite QD devices relative to their bulk counterparts, which explains the smaller V_{OC} losses observed in perovskite QDSCs. We further demonstrate that the use of colloidal Cs_xFA_{1-x}PbI₃ QDs opens an avenue towards segregation-free PSCs showing enhanced stability under continuous illumination that is beyond the reach of large-grain perovskite thin films of identical composition.

Ligand-assisted synthesis of Cs_{1-x}FA_xPbI₃ QDs

We first calculated the energies (ΔE_{ex}) required for the formation of Cs_{1-x}FA_xPbI₃ ($x=0.25, 0.50$ and 0.75) (Supplementary Fig. 1 and Supplementary Note 1) via A-site cation exchange, and the negative values suggest that this reaction is thermodynamically favourable. To prepare the alloy Cs_{1-x}FA_xPbI₃ QDs, the CsPbI₃ and FAPbI₃ QDs were first synthesized using a modified hot-injection method and then mixed in controlled molar ratios (see Methods). We took the synthesis of Cs_{0.5}FA_{0.5}PbI₃ QDs as an example to explore the feasibility of the synthetic route and closely monitored the A-site cation-exchange reaction between the parent CsPbI₃ and FAPbI₃ QDs. When the parent colloidal solutions were purified twice with methyl acetate before mixing, a large fraction of oleic acid (OA) ligands were removed, as indicated by the significant reduction of the vibration bands at $1,640\text{ cm}^{-1}$ ($-\text{C}=\text{C}-$ group) in the Fourier-transform infrared (FTIR) spectra (Supplementary Fig. 2), forming an OA-less environment. After mixing at room temperature, the two distinct peaks of CsPbI₃ and FAPbI₃ QDs did not shift obviously from their original positions within the first 30 min. Then, cation exchange occurred simultaneously in both CsPbI₃ and FAPbI₃ QDs, as suggested by the CsPbI₃ photoluminescence (PL) peaks

moving to longer wavelengths and the FAPbI₃ peaks shifting to shorter wavelengths, respectively. It took tens of hours for the two peaks to merge into one single, broad peak. Subsequently, the composition homogenization was completed in another 8 h (Fig. 1a) and the as-prepared alloy sample was denoted as Cs_{0.5}FA_{0.5}PbI₃-QD-OL. The slow reaction is in accordance with a previous report³⁶, which indicates the presence of a high kinetic barrier for cations to leave the starting QDs and diffuse into other QDs. We proposed that the OA ligands could be the key to eliminating such barriers by solvating A-site cations of QDs as highly mobile Cs-oleate and FA-oleate in the colloidal solution.

To verify this hypothesis, we intentionally kept more OA ligands in the parent colloidal solutions by performing only one purification step, thus forming an OA-rich environment. Encouragingly, the two PL peaks immediately merged into one on mixing and the resultant emission spectrum stopped changing in around 30 min, which indicates extremely rapid completion of cation exchange (Fig. 1b). Further experiments were performed to examine the critical role of OA ligands in solvating A-site cations of QDs and to validate the existence of mobile Cs-oleate and FA-oleate in colloidal solution (Supplementary Fig. 3 and Supplementary Note 2). We also checked the cation-exchange reaction in different solvents (toluene and octane), which were comparable to that in hexane (Supplementary Fig. 5). The ligand density in each colloidal QD solution was estimated (Supplementary Note 3) and is summarized in Supplementary Table 1. The as-synthesized alloy sample in the OA-rich environment was named as Cs_{0.5}FA_{0.5}PbI₃-QD-OR. Part of this sample was purified again and is denoted as Cs_{0.5}FA_{0.5}PbI₃-QD*-OR. Interestingly, we note that the alloy QDs synthesized in the OA-rich environment showed much higher PL intensity (Fig. 1c) and the corresponding PLQYs were 2–3 times higher than for those prepared in the OA-less environment (Supplementary Fig. 4 and Note 4). These results confirm our hypothesis that the noteworthy difference in ligand engineering is the key feature, which not only promotes the cation-exchange reaction, but also preserves high radiative efficiency by suppressing surface defects, as illustrated in Fig. 1d,e.

By using this ligand-assisted cation-exchange method, we then demonstrated fine-tuning of the absorption onset and PL emission peak of the alloy QDs from pure CsPbI₃ to pure FAPbI₃ (Supplementary Fig. 6). The bandgaps of each QD composition are summarized in Supplementary Table 2. All the alloy Cs_{1-x}FA_xPbI₃ QDs retain their perovskite structure, as shown in the X-ray diffraction patterns (Supplementary Fig. 7a). The enlarged view of the X-ray diffraction patterns (Supplementary Fig. 7b) indicates that the substitution of Cs⁺ with FA⁺ induces a gradual shift in the diffraction peaks, such as (200), towards a lower angle.

Scanning transmission microscopy (STEM) images (Supplementary Fig. 8a–e) reveal that all Cs_{1-x}FA_xPbI₃ QDs are uniform nanocubes with a size of $14 \pm 2\text{ nm}$. To identify the distribution of Cs and FA cations and to understand the structural evolution in atomic resolution amongst these samples, high-angle annular dark-field STEM (HAADF-STEM) characterizations were conducted (Supplementary Fig. 8f–j and Supplementary Note 5).

The Cs_{0.5}FA_{0.5}PbI₃ QD (Fig. 2a,b) was then selected as a model for structural analysis to reveal the original crystal structure of the alloy QDs. As shown in Fig. 2c,d, the observed atomic column arrangements could be regarded as the mixture of CsPbI₃ along the [001] direction and PbI₂ along the [4̄41] direction, and the area ratio between them (based on the colour-coded image, Fig. 2d) is about 1:1, consistent with the molar ratio of Cs and FA. Along the [001] direction, an atomic model (Fig. 2f) was established from the enlarged view (Fig. 2e) for the region marked with a red square in the experimental HAADF-STEM image. The simulated atomic-resolution HAADF-STEM image (Fig. 2g) via QSTEM software further confirmed the consistency between the model and the

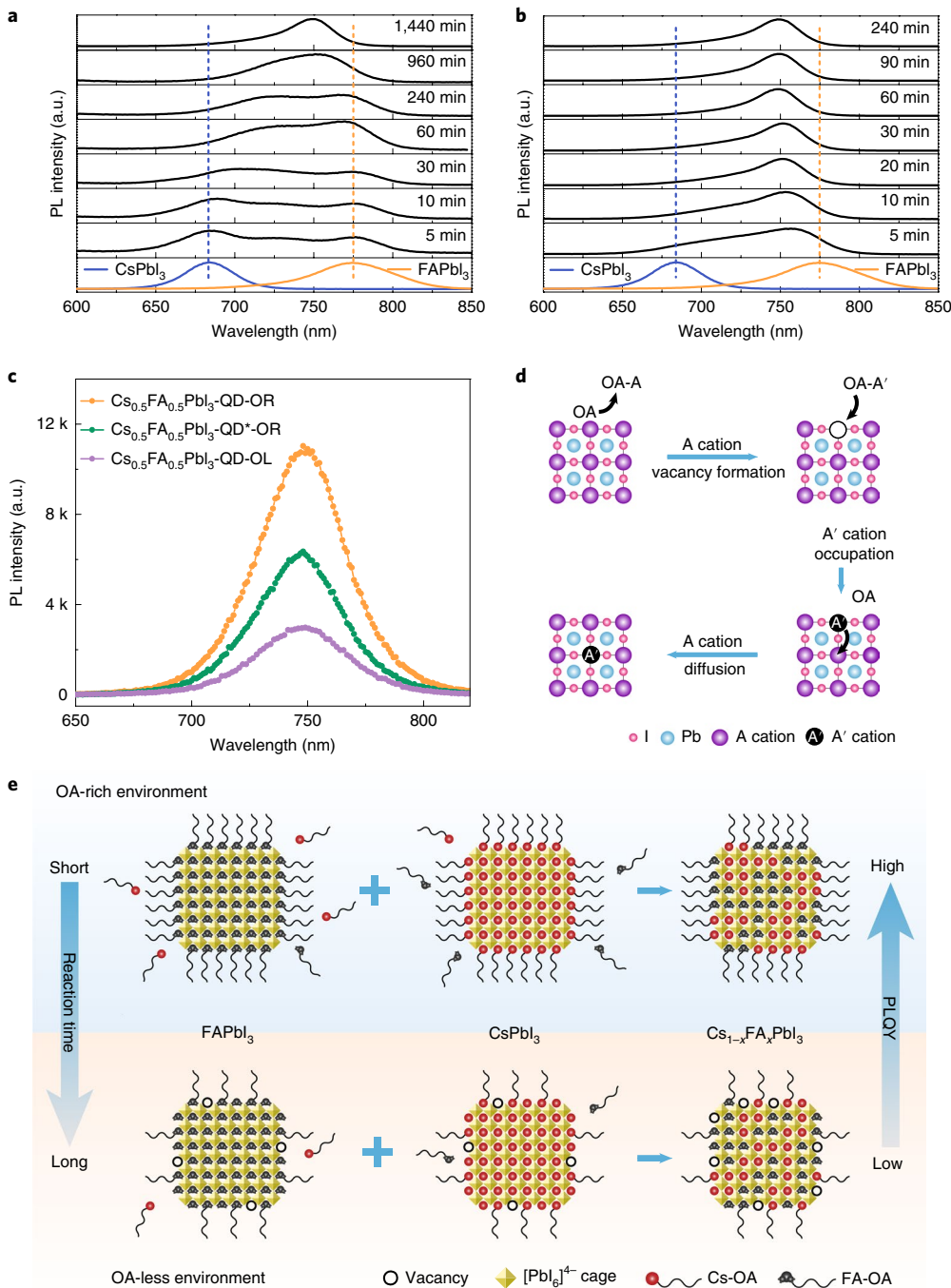


Fig. 1 | Mechanism of ligand-assisted A-site cation-exchange reaction. **a,b**, The evolution of PL emission peaks with time to form $\text{Cs}_{0.5}\text{FA}_{0.5}\text{PbI}_3$ QDs by combining parent QD solutions that were purified twice (OA-less, **a**) and once (OA-rich, **b**), respectively. The bottom-most spectra in these two figures show the individual PL emissions from CsPbI_3 (blue) and FAPbI_3 (orange). The remaining emission spectra (black) are shown for the temporal evolution with time. Before mixing, they exhibit a PL peak at 683 nm and 774 nm for CsPbI_3 (blue dashed line) and FAPbI_3 (orange dashed line), respectively. **c**, PL spectra of $\text{Cs}_{0.5}\text{FA}_{0.5}\text{PbI}_3$ -QD-OL (as-synthesized $\text{Cs}_{0.5}\text{FA}_{0.5}\text{PbI}_3$ QDs in the OA-less environment), $\text{Cs}_{0.5}\text{FA}_{0.5}\text{PbI}_3$ -QD-OR (as-synthesized $\text{Cs}_{0.5}\text{FA}_{0.5}\text{PbI}_3$ QDs in the OA-rich environment) and $\text{Cs}_{0.5}\text{FA}_{0.5}\text{PbI}_3$ -QD*-OR ($\text{Cs}_{0.5}\text{FA}_{0.5}\text{PbI}_3$ -QD-OR purified once) in hexane. **d**, Proposed A-site cation-exchange reaction mechanism. Desorption of solvated cations from QDs leaves behind cation vacancies at the surface for the new cations to occupy. **e**, Schematic illustration of cation exchange in different environments. Shuttling of FA^+ and Cs^+ cations between QDs is facilitated by the diffusion of Cs-oleate and FA-oleate in solution. As a result, the cation-exchange process under OA-rich conditions is promoted compared with that in the OA-less environment.

sample structure along this direction. Therefore, in the atomic-resolution HAADF-STEM image, the regions matching PbI_2 along the $\langle\bar{4}41\rangle$ direction with uniform atomic contrast distribution can be assigned to the original FAPbI_3 along the $[001]$ direction. The other regions with brightened-and-dimmed contrast distribution can be

assigned to CsPbI_3 along the $[001]$ direction. To confirm this, we established another model along the $[110]$ direction of $\text{Cs}_{0.5}\text{FA}_{0.5}\text{PbI}_3$ QD for structural analysis (Supplementary Fig. 9). On the basis of the models from these two directions, we restored the FAPbI_3 structure at the position of PbI_2 observed in experimental images.

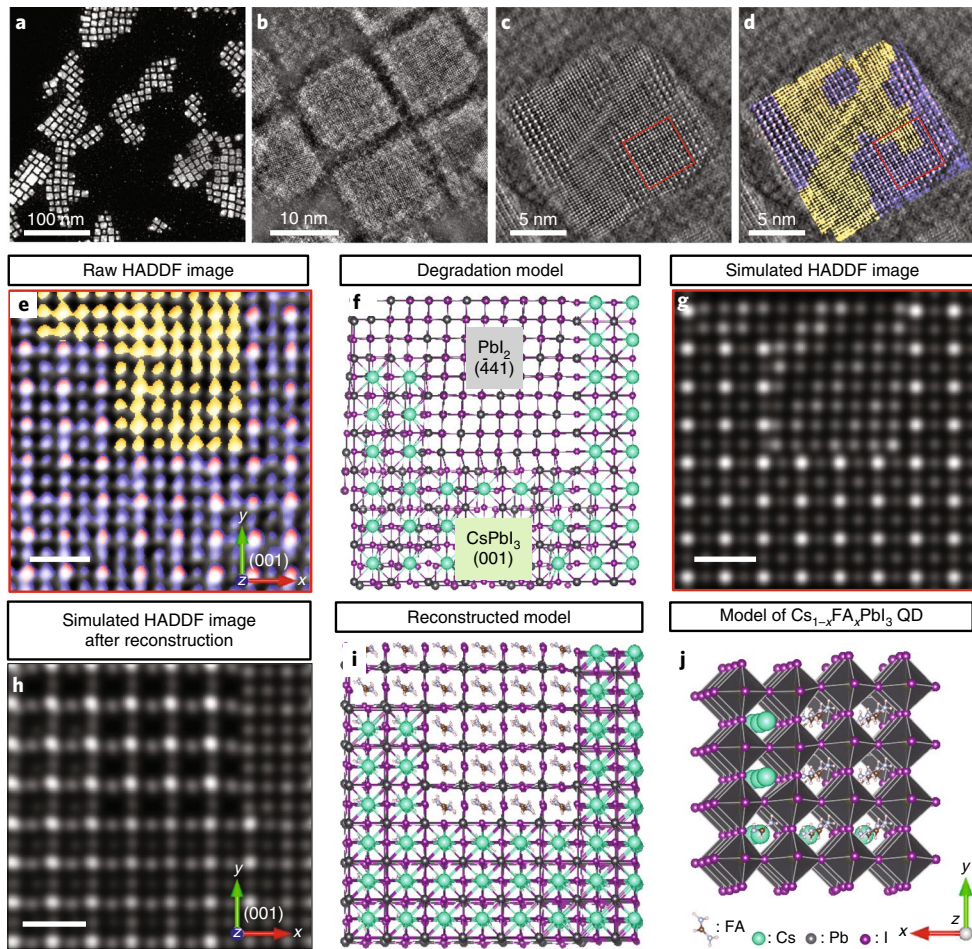


Fig. 2 | Morphology and crystal structure of $\text{Cs}_{1-x}\text{FA}_x\text{PbI}_3$ QD. **a,b**, Low-magnification (**a**) and high-magnification (**b**) HAADF-STEM images of $\text{Cs}_{0.5}\text{FA}_{0.5}\text{PbI}_3$ QDs. **c,d**, Representative atomic-resolution HAADF-STEM image (**c**) and the derived colour-coded HAADF-STEM image (**d**) of $\text{Cs}_{0.5}\text{FA}_{0.5}\text{PbI}_3$ QD. The image is viewed along the cubic [001] zone axis established from the lattice arrangement similar to the original CsPbI_3 (or FAPbI_3) cubic crystal structure. **e–g**, The enlarged view (**e**), the atomic models (**f**) and the simulated atomic-resolution HAADF-STEM image (**g**) for the region marked with a red square in **c** and **d**. In **e**, the yellow dots represent the atom column in the area with uniform contrast distribution; the pink and blue dots (pink dots represent the high-contrast atoms and blue dots represent the low-contrast atoms) represent the atom columns in the area with distinct contrast distribution. All the experimental STEM images of the samples containing FA are distorted due to decomposition of the local crystal structure from FAPbI_3 to PbI_2 under electron beam illumination. **h**, The simulated atomic-resolution HAADF-STEM image. **i**, The atomic models for the original view of $\text{Cs}_{0.5}\text{FA}_{0.5}\text{PbI}_3$ QD along the [001] zone axis after reconstruction. **j**, The established crystal structure of the $\text{Cs}_{1-x}\text{FA}_x\text{PbI}_3$ QD. Scale bar, 10 Å (**e,g,h**).

The simulated atomic-resolution HAADF-STEM image and the atomic models of the as-synthesized $\text{Cs}_{0.5}\text{FA}_{0.5}\text{PbI}_3$ QD along the [001] zone axis are shown in Fig. 2*h,i*, respectively. Thus, it is reasonable to state that the FA and Cs involved in the cation-exchange reaction were distributed among the corner-sharing PbI_6 octahedrons and grew into small FAPbI_3 and CsPbI_3 units, which assembled randomly in three dimensions to form single cubic-shaped alloy $\text{Cs}_{1-x}\text{FA}_x\text{PbI}_3$ QDs (Fig. 2*j*).

QD device architecture and performance

To investigate the role of ligand concentration in determining the quality of mixed-cation QDs, we first fabricated QDSCs using $\text{Cs}_{0.5}\text{FA}_{0.5}\text{PbI}_3$ QDs prepared in OA-rich ($\text{Cs}_{0.5}\text{FA}_{0.5}\text{PbI}_3$ -QD-OR) and OA-less environments ($\text{Cs}_{0.5}\text{FA}_{0.5}\text{PbI}_3$ -QD-OL) with pure CsPbI_3 QDs as the reference (CsPbI_3 -QD). The device configuration is shown in Supplementary Fig. 10. Figure 3*a* presents a transmission electron microscopy (TEM) cross-section image of a typical QDSC. As shown in the photocurrent density–voltage (*J*–*V*) curves (Fig. 3*b*), the CsPbI_3 -QD device had a short-circuit current density (J_{SC}) of 15.4 mA cm⁻², a V_{OC} of 1.16 V and a fill factor (FF) of 53.9%, yielding

a PCE of 9.6%. Unexpectedly, $\text{Cs}_{0.5}\text{FA}_{0.5}\text{PbI}_3$ -QD-OL devices delivered a lower J_{SC} of 14.6 mA cm⁻² and V_{OC} of 1.08 V, resulting in a PCE of 10.1%, which is comparable to the reference device. In clear contrast, a distinctly enhanced J_{SC} of 18.4 mA cm⁻² and FF of 77.9% were achieved in $\text{Cs}_{0.5}\text{FA}_{0.5}\text{PbI}_3$ -QD-OR devices, which boosted the PCE to over 16%. Detailed photovoltaic device parameters can be found in Supplementary Table 3.

Colloidal $\text{Cs}_{1-x}\text{FA}_x\text{PbI}_3$ QDs of different stoichiometry derived from the OA-rich environment were then incorporated into QDSCs to further investigate the impact of FA incorporation. Large-grain $\text{Cs}_{1-x}\text{FA}_x\text{PbI}_3$ bulk thin-film devices with the same configuration were also fabricated for comparison, and the Cs fraction was up to 25% only because of the difficulty in achieving stable compositions with higher ratios of Cs¹⁶. The corresponding *J*–*V* curves of these devices are shown in Supplementary Fig. 11. All the alloy QD devices showed negligible photocurrent hysteresis (Supplementary Fig. 12). Unlike the previous report³⁶, we observed that all the alloy $\text{Cs}_{1-x}\text{FA}_x\text{PbI}_3$ QD devices exhibited markedly increased PCEs compared with CsPbI_3 QD devices (Fig. 3*c*). The enhanced PCE is due to the improvement in J_{SC} and FF, as well as the reduction in V_{OC} loss

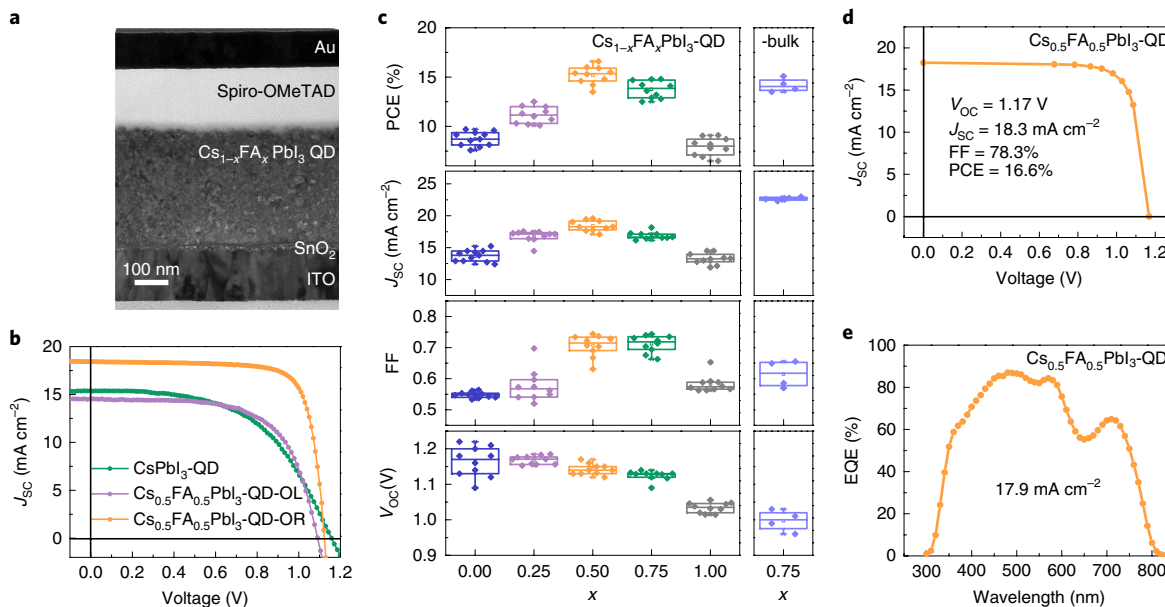


Fig. 3 | Photovoltaic performance of QD devices. **a**, Cross-section TEM image of the $\text{Cs}_{1-x}\text{FA}_x\text{PbI}_3$ QDSC. **b**, Typical J - V curves of QDSCs using different QDs. **c**, Performance evolution (PCE, J_{sc} , FF and V_{oc}) of solar cells based on $\text{Cs}_{1-x}\text{FA}_x\text{PbI}_3$ QDs of different compositions (11 devices for each composition) and bulk $\text{Cs}_{0.25}\text{FA}_{0.75}\text{PbI}_3$ (five devices). The box plot denotes median (centre line), 25th (bottom edge of the box), 75th (top edge of the box), 95th (upper whisker) and 5th (lower whisker) percentiles. The solid dots represent original data. Mixed-cation QDs were prepared in an OA-rich environment and all these PCEs were obtained on the reverse scan. **d**, Certificated J - V curve. **e**, EQE spectrum of the hero device measured at Newport PV Laboratory; the integrated J_{sc} is indicated. The J - V curve was measured under a ten-point I - V sweep configuration wherein the bias voltage (current for V_{oc} determination) is held constant until the measured current (voltage for V_{oc}) is determined to be unchanging.

(Fig. 3c). The $\text{Cs}_{0.5}\text{FA}_{0.5}\text{PbI}_3$ QDSCs delivered the best photovoltaic performance, with the average PCE increasing from ~10% to 15% on FA incorporation. A hero device fabricated with $\text{Cs}_{0.5}\text{FA}_{0.5}\text{PbI}_3$ QDs was sent to an accredited laboratory (Newport PV Laboratory) for certification. Figure 3d is the J - V curve of the hero device without encapsulation measured under a ten-point I - V sweep configuration, which is intended to represent the quasi-steady-state performance of the device. The hero device delivered a certified efficiency of 16.6% with a V_{oc} of 1.17 V, a J_{sc} of 18.3 mA cm^{-2} and a FF of 78.3% (Supplementary Figs. 13 and 14), outperforming previous QDSCs¹¹. No obvious photocurrent hysteresis was observed either in this device or other devices tested in our laboratory (Supplementary Figs. 15 and 16). The integrated J_{sc} from the external quantum efficiency (EQE) spectrum measured at Newport reached 17.9 mA cm^{-2} (Fig. 3e), which is in good agreement with that from J - V measurement. In addition, we note that all the QD devices exhibited much higher V_{oc} than those of $\text{Cs}_{0.25}\text{FA}_{0.75}\text{PbI}_3$ -Bulk devices (Fig. 3b), as well as other reported $\text{Cs}_{1-x}\text{FA}_x\text{PbI}_3$ -Bulk devices^{12,14,15}.

Synergistic effect of ligand and FA on defect reduction

All mixed-cation $\text{Cs}_{1-x}\text{FA}_x\text{PbI}_3$ QDs derived in the OA-rich environment delivered enhanced PV performance relative to CsPbI_3 QDs, which we tentatively ascribe to their enhanced light harvesting and reduced defect density. The broader spectral absorption with incorporation of FA (Supplementary Fig. 6a) is apparently the key reason for the improved light harvesting, resulting in higher J_{sc} . However, deteriorated J_{sc} and V_{oc} were observed in the device with $\text{Cs}_{0.5}\text{FA}_{0.5}\text{PbI}_3$ QDs prepared under the OA-less condition. To uncover the origin of such a distinct difference, we first performed time-resolved PL (TRPL) decay measurements on various QD films. A much longer carrier lifetime of 97 ns was deduced from the fitted TRPL decay curve of the $\text{Cs}_{0.5}\text{FA}_{0.5}\text{PbI}_3$ -QD-OR film, which was more than three times longer than that (26 ns) of the CsPbI_3 -QD film (Fig. 4a). This is consistent with previous studies showing that

incorporation of an FA cation leads to longer carrier lifetime and reduced non-radiative recombination^{32,33}. However, no obvious lifetime increase was observed in the $\text{Cs}_{0.5}\text{FA}_{0.5}\text{PbI}_3$ -QD-OL film. We speculate that this is because the insufficient coverage of surface ligands on the parent CsPbI_3 and FAPbI_3 QDs could easily generate undesirable defects either before or during the cation-exchange reaction, given their vulnerable nature in polar solvent and ambient air, which was confirmed by further HAADF-STEM analysis (Supplementary Fig. 17). Therefore, the extended charge-recombination lifetime observed in the $\text{Cs}_{0.5}\text{FA}_{0.5}\text{PbI}_3$ -QD-OR sample should be ascribed to the synergistic effect of ligand and FA in suppressing the formation of deep-trap defects that cause non-radiative trap-assisted recombination.

To confirm the defect reduction, we then performed space charge-limited current (SCLC) measurements on hole-only devices with different QDs (Fig. 4b). In all cases, a linear (ohmic) rise at lower voltages was observed, followed by a logarithmic slope greater than 3 as the voltage increases. This is indicative of trap-filling, and the cross-over voltage (V_{TFI}) between the two slopes is often taken as the trap-filling voltage, from which the trap density can at least be estimated. While this approach is quite robust for single crystals (that are electrically thick), we would caution that the trap-filling voltage is subject to considerable uncertainty in thin-film diodes because of the finite shunt resistance due to the inevitable defects and pin holes, which impact the initial ohmic part of the current rise. However, what can be seen from these measurements is that the trap-filling occurs in relative terms at lower voltages in $\text{Cs}_{0.5}\text{FA}_{0.5}\text{PbI}_3$ -QD-OR devices versus CsPbI_3 -QD and $\text{Cs}_{0.5}\text{FA}_{0.5}\text{PbI}_3$ -QD-OL devices, indicating lower trap density, which leads to significant FF improvement and smaller V_{oc} loss in the corresponding QDSCs. Again, this indicates that an OA-rich environment is essential for achieving significant defect reduction by FA incorporation. To further understand the mechanism of FA-induced deep-trap defect reduction, we calculated the formation

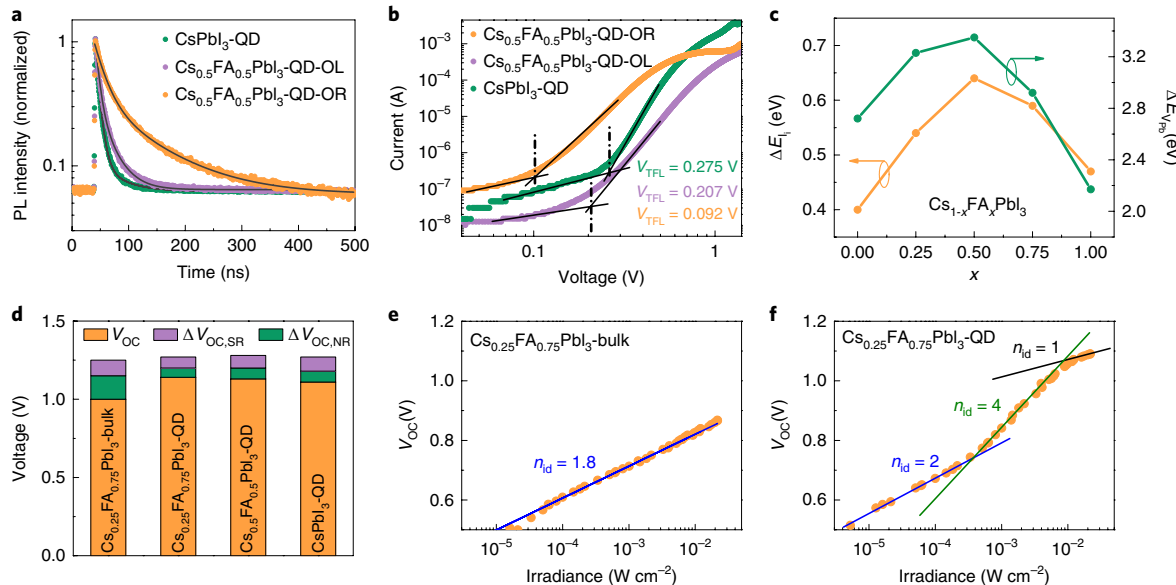


Fig. 4 | Optoelectronic characteristics of QD thin films and V_{OC} loss mechanism in QD devices. **a**, TRPL spectra of $CsPbI_3$ -QD, $Cs_{0.5}FA_{0.5}PbI_3$ -QD-OL and $Cs_{0.5}FA_{0.5}PbI_3$ -QD-OR thin films on glass substrates. The curves are fitted with a bi-exponential decay function. **b**, J-V characteristics of hole-only devices (ITO/PEDOT:PSS/QD/Spiro-OMeTAD/Au), used for estimating the SCLC defect concentration of samples in **a**. In the J-V curve, the cross-over voltage between the ohmic and logarithmic slopes is taken as the trap-filling voltage (V_{TFL}). The solid black lines indicate guides to the eye for the specified V_{TFL} . **c**, Formation energy of I_i (ΔE_{I_i}) and V_{pb} ($\Delta E_{V_{pb}}$) of $Cs_{1-x}FA_xPbI_3$ with different x values. **d**, Voltage loss due to the surface recombination and non-radiative recombination in bulk and QD devices. **e,f**, Light intensity-dependent V_{OC} measurements over a large dynamic range in $Cs_{0.25}FA_{0.75}PbI_3$ -Bulk device (**e**) and $Cs_{0.25}FA_{0.75}PbI_3$ -QD device (**f**). The solid lines denote linear fits to the experimental data and the ideality factors (n_{id}) are provided in the panels. The mixed-cation QDs in **d** and **f** were derived in an OA-rich environment.

energy of two typical defects, iodide interstitial (I_i) and lead vacancy (V_{pb}) as a proof-of-concept. The I_i and V_{pb} defects have been demonstrated as the most important deep-trap defects in perovskite materials that are mainly responsible for the charge-recombination processes^{39,40}. The optimized defect structures of I_i and V_{pb} on the $Cs_{1-x}FA_xPbI_3$ are shown in Supplementary Figs. 18 and 19. Figure 4c summarizes the formation energy of I_i (ΔE_{I_i}) and V_{pb} ($\Delta E_{V_{pb}}$) for different compositions, and $Cs_{0.5}FA_{0.5}PbI_3$ shows the highest formation energy for both types of defects. The positive values reveal that the defect formation in all compositions is an endothermic process. Compared with $CsPbI_3$ and $FAPbI_3$, the higher formation energy explains why it is more difficult to form deep-trap defects, such as I_i and V_{pb} , in mixed-cation $Cs_{1-x}FA_xPbI_3$ ($x=0.25, 0.50$ and 0.75 , respectively) perovskites, which is qualitatively consistent with the experimental results.

Mechanistic study of V_{OC} loss in QD devices

The more optimal V_{OC} deficit observed in QD devices relative to bulk devices led us to consider what could be unique about perovskite QDs in suppressing V_{OC} losses. The V_{OC} of a solar cell can be written in terms of radiative ($\Delta V_{OC,R}$), non-radiative ($\Delta V_{OC,BNR}$) and surface recombination ($\Delta V_{OC,SR}$) losses relative to the bandgap:

$$V_{OC} = E_g/q - \Delta V_{OC,R} - \Delta V_{OC,BNR} - \Delta V_{OC,SR} \quad (1)$$

where E_g is the bandgap and q is the elementary charge.

We note that surface recombination is also a non-radiative process. As such, we distinguish it from bulk non-radiative recombination to explain the V_{OC} improvements. $\Delta V_{OC,SR}$ is defined by the difference between the quasi-Fermi level splitting ($\mu = E_{fn} - E_{fp}$, where E_{fn} is the electron quasi-Fermi level and E_{fp} is the hole quasi-Fermi level) in the bulk of the semiconductor and contacts:

$$q\Delta V_{OC,SR} = \mu_{\text{bulk}} - \mu_{\text{contact}} = \mu_{\text{bulk}} - qV_{OC} \quad (2)$$

To determine μ_{bulk} , the PLQY was determined⁴¹ under V_{OC} conditions using a small perturbation approach (Supplementary Note 6). PLQY values as large as 10% were obtained (at 1-sun equivalent), meaning reduced non-radiative losses versus the bulk perovskite cells. The values of V_{OC} , μ_{bulk} , $j_{0,R}$ (radiative saturation dark current, Supplementary Note 6), $\Delta V_{OC,BNR}$ and $\Delta V_{OC,SR}$ for the bulk and QD devices derived from this analysis are given in Supplementary Table 4. Figure 4d shows the voltage loss due to the surface recombination and non-radiative recombination in bulk and QD devices: $\Delta V_{OC,NR}$ decreased from 150 meV to 60 meV with a 30 meV reduction in $\Delta V_{OC,SR}$. We attribute the reduction in the surface recombination to the reduced trap density in QD devices lowering the surface recombination velocity induced by mid-gap trap states near the contact. Similar values are observed for $x=0.5$. These data also indicate that by the use of perfectly selective contacts the V_{OC} of these QDSCs can be improved to 1.2 V, which is only 70 meV lower than the radiative limit (Supplementary Table 4).

In a deeper analysis (Fig. 4e,f), light intensity-dependent V_{OC} measurements over a large dynamic range revealed that recombination in both $Cs_{0.25}FA_{0.75}PbI_3$ -Bulk and $Cs_{0.25}FA_{0.75}PbI_3$ -QD devices was trap-assisted dominated with ideality factors (n_{id}) close to 2. By increasing the light intensity, we observed that the bulk device remained trap-limited ($n_{id} \approx 2$), whereas the V_{OC} in the QD device increased sharply (with an n_{id} of 4 within an intermediary intensity range for an unknown reason) before reaching a new regime with n_{id} of 1 (band-to-band recombination-dominated). From both results it can be concluded that the recombination is predominantly trap-assisted in both bulk and QD devices at low light intensities, whereas at high light intensities band-to-band recombination in QD devices is dominant, hence the larger PLQY and n_{id} of 1. This distinct property might be the key origin of the reduced V_{OC} loss observed in QD devices.

Stability of $Cs_{1-x}FA_xPbI_3$ QD films and devices

We first evaluated the QD device stability under ambient conditions. The PCE evolutions of both $CsPbI_3$ and $Cs_{0.5}FA_{0.5}PbI_3$ QDSCs

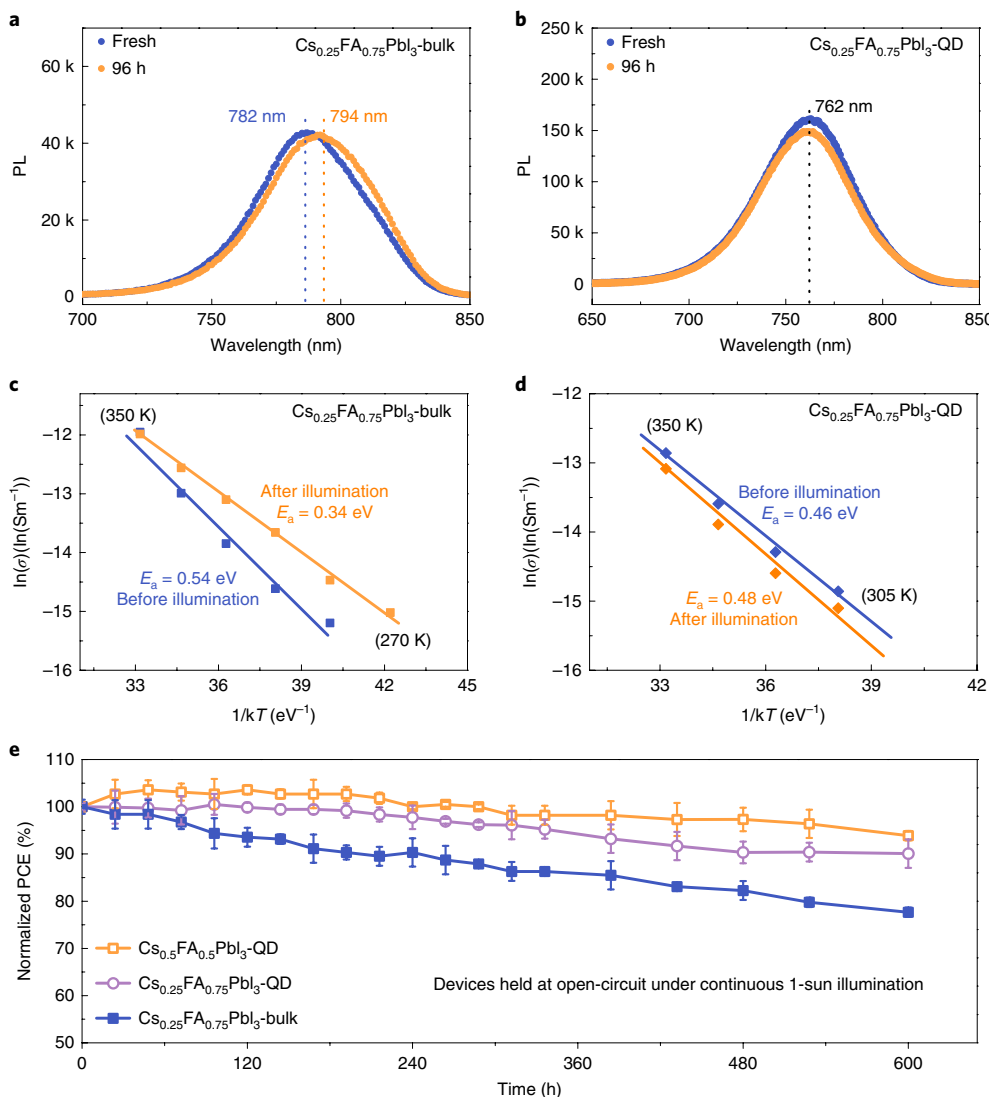


Fig. 5 | Stability of QD thin film and devices. **a,b**, PL spectra of $\text{Cs}_{0.25}\text{FA}_{0.75}\text{PbI}_3$ -Bulk film (**a**) and $\text{Cs}_{0.25}\text{FA}_{0.75}\text{PbI}_3$ -QD film (**b**) on SnO_2 -coated ITO substrates before and after illumination for 96 h in N_2 , respectively. The wavelengths of the PL peaks are indicated in the panel. **c,d**, Arrhenius plots of the ion conductivity of $\text{Cs}_{0.25}\text{FA}_{0.75}\text{PbI}_3$ -Bulk film (**c**) and $\text{Cs}_{0.25}\text{FA}_{0.75}\text{PbI}_3$ -QD film (**d**) before and after illumination (25 mW cm^{-2}) for 3 h, respectively, from the slope of which the activation energy for ion migration is calculated according to the Arrhenius equation. The solid lines are linear fits. The temperature changed from 270 K to 350 K and was well controlled with a variation less than 0.1 K during measurement. **e**, Long-term stability of unencapsulated solar cells fabricated with $\text{Cs}_{0.25}\text{FA}_{0.75}\text{PbI}_3$ -Bulk film, $\text{Cs}_{0.25}\text{FA}_{0.75}\text{PbI}_3$ -QD film and $\text{Cs}_{0.5}\text{FA}_{0.5}\text{PbI}_3$ -QD film monitored at open circuit under 1-sun illumination in N_2 atmosphere (the device temperature was measured to be $-50\text{--}65^\circ\text{C}$). Mixed-cation QDs were derived from an OA-rich environment. Each average (symbol) and standard deviation (error bar) was calculated on the basis of three device-testing results.

without encapsulation were monitored over a long storage time-scale in ambient air (relative humidity of 50–70%). The CsPbI_3 QD device degraded rapidly and lost the majority of its efficiency within four days (Supplementary Fig. 21). In strong contrast, the $\text{Cs}_{0.5}\text{FA}_{0.5}\text{PbI}_3$ QD device retained over 97% of its original efficiency after storage for 20 days.

It is generally accepted that the formation and migration of ionic defects within the halide perovskite lattice are potential sources of intrinsic degradation for perovskite devices^{18,42}. Therefore, we anticipate that the significant defect reduction demonstrated for alloy $\text{Cs}_{1-x}\text{FA}_x\text{PbI}_3$ QD films would contribute enhancement of the device stability under illumination. We first checked the stability of QD films by monitoring their PL emission changes before and after continuous light irradiation in nitrogen. The $\text{Cs}_{0.25}\text{FA}_{0.75}\text{PbI}_3$ -QD and $\text{Cs}_{0.25}\text{FA}_{0.75}\text{PbI}_3$ -Bulk films were fabricated for easy comparison. The QD film showed a significant blue shift in the PL peak

position compared with the bulk film, due to quantum confinement. Under continuous illumination for 96 h, the PL emission peak had a red shift of 12 nm in a $\text{Cs}_{0.25}\text{FA}_{0.75}\text{PbI}_3$ -Bulk thin film (Fig. 5a). Such emission changes originate from light-induced cation migration and segregation in bulk perovskite, which could lead to device burn-in and accelerate the degradation of PSCs operated in an inert atmosphere¹⁸. Encouragingly, we found that the $\text{Cs}_{0.25}\text{FA}_{0.75}\text{PbI}_3$ -QD film exhibited negligible change in PL emission (Fig. 5b), suggesting suppressed ion migration in QD films. To confirm this, we performed ion conductivity measurements on lateral devices fabricated with $\text{Cs}_{0.25}\text{FA}_{0.75}\text{PbI}_3$ -Bulk and -QD films. As shown in Fig. 5c, the activation energy (E_a) for ion migration in $\text{Cs}_{0.25}\text{FA}_{0.75}\text{PbI}_3$ -Bulk film drops from 0.54 eV to 0.34 eV after illumination, indicating a reduced energy barrier for ions to move. However, the E_a for ion migration in the QD film does not change obviously after illumination (Fig. 5d), which suggests that light irradiation does not intensify

ion migration in QD films. This is consistent with recent studies showing that lowering the diffusion length tends to decrease the rate of segregation, and both theoretical and experimental results indicate a segregation-free region for perovskites with a certain grain size below the threshold of 46 ± 7 nm (refs. ^{43,44}). The remaining capping ligands that passivate the surface of QDs may also contribute to the reduction of defect-mediated ion migration.

We further examined the long-term stability of QD devices under illumination. Completed devices without encapsulation were held at open circuit under continuous 1-sun illumination without cooling in nitrogen. The reference $\text{Cs}_{0.25}\text{FA}_{0.75}\text{PbI}_3$ -Bulk device quickly lost over 20% of its initial efficiency after 600 h (Fig. 5e). In sharp contrast, the $\text{Cs}_{0.25}\text{FA}_{0.75}\text{PbI}_3$ -QD and $\text{Cs}_{0.5}\text{FA}_{0.5}\text{PbI}_3$ -QD devices retained 90% and 94% of their original PCEs, respectively, because of their coupled V_{OC} and FF stability (Supplementary Fig. 22). The enhanced stability in QDSCs compared with bulk devices could be ascribed to their improved phase stability under continuous illumination, which we believe is closely related to the suppressed ion migration within QD films. We expect further improvement in efficiency and operational stability of QDSCs with more stable hole-transport materials and appropriate interface engineering.

Conclusion

In summary, we have developed an effective OA ligand-assisted cation-exchange strategy that enables controllable synthesis of mixed-cation $\text{Cs}_{1-x}\text{FA}_x\text{PbI}_3$ QDs with remarkable ambient stability. We show that the cross-exchange of cations is facilitated in an OA-rich environment, leading to rapid formation of $\text{Cs}_{1-x}\text{FA}_x\text{PbI}_3$ QDs with reduced defect density. Solar cells fabricated with $\text{Cs}_{1-x}\text{FA}_x\text{PbI}_3$ QDs exhibit reduced voltage losses compared with those using CsPbI_3 QDs and corresponding bulk perovskite cells, yielding a certified record PCE of 16.6% for QDSCs. The suppressed phase segregation in $\text{Cs}_{1-x}\text{FA}_x\text{PbI}_3$ QDs accounts for the superior photostability of QDSCs over their counterpart bulk devices. We anticipate that colloidal $\text{Cs}_{1-x}\text{FA}_x\text{PbI}_3$ QDs will pave the way for next-generation PVs and optoelectronics with improved stability and flexibility.

Methods

Chemicals. All chemicals were purchased from Sigma Aldrich and used without purification, unless otherwise noted. Caesium carbonate (Cs_2CO_3 , 99.9%), lead (II) iodide (PbI_2 , 99.998%, Alfa Aesar), oleic acid (technical grade 90%), oleylamine (OLA, technical grade 70%), 1-octadecene (ODE, technical grade 90%), toluene (anhydrous 99.8%), hexane (reagent grade $\geq 95\%$), octane (anhydrous, $\geq 99\%$), methyl acetate (MeOAc, anhydrous 99.5%), ethyl acetate (EtOAc, anhydrous 99.5%), lead(II) acetate trihydrate ($\text{Pb}(\text{OAc})_2 \cdot 3\text{H}_2\text{O}$, 99.999%), formamide acetic acid salt ($\geq 99\%$), oleyl ammonium iodide (OLA-I, $\geq 99\%$, Xi'an Baolaite), lead(II) nitrate ($\text{Pb}(\text{NO}_3)_2$, 99.999%), rhodamine 6G (99%), ethanol (EtOH, Merck, $\geq 99.5\%$), SnO_2 nanoparticle dispersion (15% in H_2O , Alfa Aesar), (2,2',7,7'-tetrakis(*N,N*-di-*p*-methoxyphenylamine)-9,9'-spirobifluorene (spiro-OMeTAD, $\geq 99.5\%$, Xi'an Baolaite), chlorobenzene (anhydrous, 99.8%), 4-*tert*-butylpyridine (96%, Aldrich), bis(trifluoromethane)sulfonimide lithium salt (Li-TFSI) and acetonitrile (anhydrous, 99.8%).

Synthesis of colloidal $\text{Cs}_{1-x}\text{FA}_x\text{PbI}_3$ QDs. CsPbI_3 QDs were synthesized following the previous report⁴⁵ with some modification. Cs-oleate was obtained by dissolving 0.1 g Cs_2CO_3 into 0.4 ml OA and 10 ml ODE, and the mixture was loaded into a 50-mL three-neck flask and stirred under vacuum for 30 min at 120 °C. After fully dissolving, the Cs-oleate in ODE was stored under nitrogen until it was used. PbI_2 (0.4 g), ODE (20 ml), OA (2 ml) and OLA (2 ml) were stirred in a 100-mL flask and degassed under vacuum at 120 °C for 1 h. The flask was then filled with N_2 and kept under constant N_2 flow. The temperature was increased to 170 °C, then 3.2 mL of the Cs-oleate (~0.063 M) precursor was swiftly injected into the mixture. After 5–10 s, the reaction was quenched by immediate immersion of the flask into an ice bath. After cooling to room temperature, 30 mL of MeOAc was added, and the mixture was centrifuged at 8,000 r.p.m. for 5 min. The resulting QD precipitate was dispersed in hexane with a concentration of 50 mg mL⁻¹ and stored under nitrogen until use.

FAPbI_3 QDs were synthesized following the previous report³⁴. $\text{Pb}(\text{acetate})_2 \cdot 3\text{H}_2\text{O}$ (0.152 g), FA-acetate (0.157 g), ODE (16 mL) and OA (4 mL) were added in a 25-mL three-neck flask and dried under vacuum for 30 min at 40 °C. The mixture was then heated to 80 °C under N_2 atmosphere, followed by injection of

OLA-I (0.474 g dissolved in 4 mL of toluene). After 30 s, the reaction mixture was cooled in the water bath. After cooling to room temperature, 20 mL of MeOAc was added, and the mixture was centrifuged at 8,000 r.p.m. for 5 min. The resulting QD precipitate was dispersed in hexane with a concentration of 50 mg mL⁻¹ and stored under nitrogen for further use.

For the cation-exchange reactions conducted in OA-rich environment, the stored CsPbI_3 and FAPbI_3 QDs were purified once with MeOAc. Their molar concentrations were determined before mixing in controlled ratios. The ligand-assisted cation-exchange reaction was completed in 30–60 min at room temperature. We note that this ligand-assisted cation-exchange technique is versatile and very efficient, and could be easily integrated with high-volume QD manufacturing platforms such as a continuous-flow microfluidic reactor³⁵. The resultant mixed-cation QDs were purified by adding EtOAc (volume ratio of QD solution to EtOAc was 1:2) and centrifuged at 8,000 r.p.m. for 5 min. This process was repeated once more to further purify the QDs. Finally, octane was added to disperse the QDs to a concentration around 60 mg mL⁻¹ for solar cell fabrication. For the cation-exchange reactions conducted in the OA-less environment, the stored CsPbI_3 and FAPbI_3 QDs were purified twice with MeOAc before mixing and the reaction took over 48 h.

Device fabrication. Glass/indium-doped tin oxide (ITO) substrates were cleaned with successive sonication in 2-propanol, acetone and 2-propanol, each for 15 min, respectively. The cleaned substrates were further treated in an ultraviolet–ozone chamber before use. The SnO_2 colloidal solution (Alfa Aesar) was diluted by H_2O to 1.5% and spin-coated onto glass/ITO substrates at 3,000 r.p.m. for 30 s, and then baked on a hot plate in air at 150 °C for 30 min.

For QD films, first, saturated $\text{Pb}(\text{NO}_3)_2$ in MeOAc solution and FAI in EtOAc solution were prepared. For the thin-film fabrication process, the QDs (~60 mg mL⁻¹ in octane) were spin-coated on SnO_2 substrate at 2,000 r.p.m. for 30 s, and then swiftly dipped in the $\text{Pb}(\text{NO}_3)_2$ solution. The saturated $\text{Pb}(\text{NO}_3)_2$ solution was used to maintain the surface structure of the QDs by alleviating the dissolving of lead atoms from QDs during the removal of long-chain ligands. The film was rinsed using neat, anhydrous MeOAc and then dried with a stream of air. This procedure was repeated four times. The films were then soaked in the FAI solution for 10 s to enhance the electronic coupling, which was followed by rinsing with MeOAc and drying²⁹. Deposition of all QD films was performed in air (relative humidity, <40%).

As for bulk $\text{Cs}_x\text{FA}_{1-x}\text{PbI}_3$ films, FAI (1 M) with excess of PbI_2 (1.1 M) was dissolved in a mixed solvent of DMF and DMSO (1:4 v/v), followed by addition of CsI stock solution (1.5 M in DMSO) to achieve the desired composition. The perovskite precursor was spin-coated on SnO_2 substrates at 2,000 r.p.m. for 10 s and 6,000 r.p.m. for 30 s, during which 200 μl of chlorobenzene was dropped on the spinning substrate 15 s before the end of second step. The substrates were then annealed on a hot plate at 65 °C for 10 min and 100 °C for 60 min to obtain crystalline perovskite films.

Finally, the spiro-OMeTAD solution was prepared by dissolving 73.5 mg of spiro-OMeTAD in 1 mL of chlorobenzene, and then 28.8 μl of 4-*tert*-butylpyridine and 17.5 μl of Li-TFSI (520 mg mL⁻¹ in acetonitrile) solution was added. The spiro-OMeTAD solution was spin-coated onto the QD or bulk perovskite films at 4,000 r.p.m. for 30 s. The gold electrode was then deposited by thermal evaporation at 0.5 Å s⁻¹ for a total thickness of 80 nm.

Structure and optical characterizations. Ultraviolet–visible absorption spectra for colloidal solutions were collected using a Jasco V670 spectrometer in transmission mode. Powder X-ray diffraction patterns were obtained with a STOE STADI P powder diffractometer. A germanium monochromator, CuK α irradiation and a silicon strip detector (Dectris Mythen) were used. The functional groups of the films were characterized by an FTIR spectrometer (Nicolet 5700 FTIR) with an attenuated total reflection accessory. The steady-state PL emissions from QD solutions and films were measured at 450-nm light source excitation using a monochromatized Xe lamp, and the TRPL decay studies were carried out with a 377-nm pulsed diode laser excitation source on a fluorescence spectrophotometer (FLSP-900, Edinburgh Instruments). The PLQYs of the QD solutions were estimated according to standard procedure using rhodamine 6G as a reference dye⁴⁶. The TRPL curves were fitted with a bi-exponential function of time (t):

$$F(t) = A_1 e^{-\frac{t}{\tau_1}} + A_2 e^{-\frac{t}{\tau_2}} + y_0 \quad (3)$$

where A_1 and A_2 are prefactors while τ_1 and τ_2 represent the time constant, and y_0 is a constant⁴⁷.

Scanning electron microscopy and STEM. STEM examination was carried out using a probe-corrected JEOL ARM200F equipped with a cold-field emission gun operating at an acceleration voltage of 200 kV. HAADF images were acquired with inner and outer collection angles of 68 and 280 mrad, respectively, ensuring Z-contrast, while bright-field images were acquired with a maximum collection angle of 17 mrad. All images (1,024 \times 1,024 pixels) were acquired with a dwell time of 10 ms per pixel and a convergence angle of 25 mrad, resulting in a probe size of about 0.1 nm and a current of 26.4 pA. Images were processed by the Gatan Digital

Micrograph software with the following steps: spatial filter was used to smooth the image first, and then we combine the FFT filter with the mask tool to get rid of the noise. We also used the deconvolution tool to increase the quality of the images. QSTEM software was used to simulate the HAADF-STEM images of $\text{Cs}_{0.5}\text{FA}_{0.5}\text{PbI}_3$ along the different zone axes. The input parameters were set according to the experimental conditions. Probe size, convergence angle and acceptance angle of the ADF detector were critical and are accounted for in the image simulation.

The cross-section lamellae of the solar cell device were prepared with a Scios DualBeam focused ion beam scanning electron microscope (FEI) system. Images were obtained with a FEI F20 FEG-S/TEM instrument.

Solar cell testing. The J - V curves were measured with a source meter (Keithley 2420) using a solar simulator (Newport, Oriel Class AAA, 94063A) at 100 mW cm^{-2} illumination (AM 1.5G) equipped with a calibrated silicon reference cell and meter (Newport, 91150V) certified by the National Renewable Energy Laboratory. The J - V curves were measured in reverse scan (from 1.3 V to -0.1 V) and forward scan (from -0.1 V to 1.3 V) modes at a scan speed of 100 mV s^{-1} with a delay time of 100 ms . There was no preconditioning before measurement. A metal shadow mask (0.058 cm^2) was used to define the active area of devices, and all devices (including the device tested in Newport PV Laboratory) were measured in ambient air without anti-reflection layer. For long-term photostability testing, the unsealed devices were illuminated under continuous 100 mW cm^{-2} irradiation by a LED grow light (Spectrum King MLH140) under open circuit condition in an N_2 atmosphere.

Space charge-limited current. SCLC I-V measurements were performed on devices with structures of ITO/PEDOT:PSS/QDs/spiro-OMeTAD/Au. For device fabrication, the PEDOT:PSS solution was filtered through a $0.45\text{-}\mu\text{m}$ PTFE filter and spin-coated onto ITO at $4,000 \text{ r.p.m.}$ for 60 s . Afterwards, the film was baked on a hot plate in air at 150°C for 30 min . The other layers were fabricated using the same procedure as for solar cell device fabrication. Current, as a function of the applied voltage, was measured using IVIUMnSTAT in the dark. A non-linear response was observed and analysed according to SCLC theory⁴⁸.

Ion conductivity. Lateral devices with a configuration of ITO/Bulk perovskite or QD film/Au were fabricated for ion conductivity measurements. The QD films were prepared following the same procedure as that for QDSC fabrication. The ion conductivity (σ) was extracted from the current changes of a lateral device under a $0.35 \text{ V }\mu\text{m}^{-1}$ electrical field, and the activation energy for ion migration was obtained by fitting the ion conductivity at different temperatures according to the Arrhenius equation⁴⁹.

Light intensity-dependent photovoltage. For light intensity-dependent V_{OC} measurements, the voltage at an applied device current of $I=0$ (open circuit) was measured at an illumination wavelength of 520 nm (Oxxius laser diode) as a function of light irradiance. Before light coupling into an integrating sphere (Thorlabs, IS236A-4), two combined filter wheels containing different optical density filters attenuated the light irradiance over a dynamic range of 70 dB . The integrating sphere was used to simultaneously record the V_{OC} using a source meter unit (Keithley 2450) and to record the incident light irradiance with a silicon photodiode sensor (Thorlabs, SM05PD1A). For the light irradiance calibration, a Thorlabs NIST-calibrated silicon photodiode sensor (S121C) was used.

Solar cell PLQY. A background continuous-wave light source was used to bring the solar cell to 1-sun equivalent condition, at which V_{OC} and J_{SC} are approximately equal to those determined at AM 1.5G. The wavelength of the laser was 520 nm (Oxxius laser diode). A small perturbation (less than 1% of the continuous-wave background light) was imposed to the background light at a modulation frequency of 7 Hz . Integrated photoluminescence was measured using a silicon photodetector (SM1PD1B) and long-pass filters at 550 nm and 650 nm to eliminate the scattered pump. The photodetector signal was preamplified using a Femto DHPCA-100 at a gain of 10^7 V A^{-1} and then recorded using a Spectrum Analyser (Keysight N9010A) at a resolution bandwidth of 1 Hz . The PL signal was at least 40 dB larger than the electrical noise floor and stray pump laser. The photodetector current was then converted to the photon flux received at the photodetector position. The total flux emitted by the device was calculated on the basis of a nearly Lambertian emission and photodetector flux. The PLQY was determined from the total flux and the intensity of the modulated pump. During the measurement, the solar cell was under open circuit condition.

Reporting Summary. Further information on research design is available in the Nature Research Reporting Summary linked to this article.

Data availability

The data that support the plots within this paper and other findings of this study are available from the corresponding authors on reasonable request.

Received: 24 July 2019; Accepted: 28 November 2019;
Published online: 20 January 2020

References

- Kojima, A., Teshima, K., Shirai, Y. & Miyasaka, T. Organometal halide perovskites as visible-light sensitizers for photovoltaic cells. *J. Am. Chem. Soc.* **131**, 6050–6051 (2009).
- Kim, H.-S. et al. Lead iodide perovskite sensitized all-solid-state submicron thin film mesoscopic solar cell with efficiency exceeding 9%. *Sci. Rep.* **2**, 591 (2012).
- Lee, M. M., Teuscher, J., Miyasaka, T., Murakami, T. N. & Snaith, H. J. Efficient hybrid solar cells based on meso-superstructured organometal halide perovskites. *Science* **338**, 643–647 (2012).
- Burschka, J. et al. Sequential deposition as a route to high-performance perovskite-sensitized solar cells. *Nature* **499**, 316–319 (2013).
- Lin, K. et al. Perovskite light-emitting diodes with external quantum efficiency exceeding 20 per cent. *Nature* **562**, 245–248 (2018).
- Cao, Y. et al. Perovskite light-emitting diodes based on spontaneously formed submicrometre-scale structures. *Nature* **562**, 249–253 (2018).
- Xing, G. et al. Low-temperature solution-processed wavelength-tunable perovskites for lasing. *Nat. Mater.* **13**, 476–480 (2014).
- Zhu, H. et al. Lead halide perovskite nanowire lasers with low lasing thresholds and high quality factors. *Nat. Mater.* **14**, 636–642 (2015).
- Jeon, N. J. et al. Compositional engineering of perovskite materials for high-performance solar cells. *Nature* **517**, 476–480 (2015).
- Jiang, Q. et al. Surface passivation of perovskite film for efficient solar cells. *Nat. Photonics* **13**, 460–466 (2019).
- Best research-cell efficiencies chart. NREL <https://www.nrel.gov/pv/cell-efficiency.html> (2019).
- Lee, J.-W. et al. Formamidinium and cesium hybridization for photo- and moisture-stable perovskite solar cell. *Adv. Energy Mater.* **5**, 1501310 (2015).
- Huang, J., Xu, P., Liu, J. & You, X.-Z. Sequential introduction of cations deriving large-grain $\text{Cs}_x\text{FA}_{1-x}\text{PbI}_3$ thin film for planar hybrid solar cells: insight into phase-segregation and thermal-healing behavior. *Small* **13**, 1603225 (2017).
- Turren-Cruz, S.-H., Hagfeldt, A. & Saliba, M. Methylammonium-free, high-performance, and stable perovskite solar cells on a planar architecture. *Science* **362**, 449–453 (2018).
- Saliba, M. et al. Incorporation of rubidium cations into perovskite solar cells improves photovoltaic performance. *Science* **354**, 206–209 (2016).
- Li, Z. et al. Stabilizing perovskite structures by tuning tolerance factor: formation of formamidinium and cesium lead iodide solid-state alloys. *Chem. Mater.* **28**, 284–292 (2016).
- Kubicki, D. J. et al. Phase segregation in potassium-doped lead halide perovskites from ^{39}K solid-state NMR at 21.1 T . *J. Am. Chem. Soc.* **140**, 7232–7238 (2018).
- Domanski, K. et al. Migration of cations induces reversible performance losses over day/night cycling in perovskite solar cells. *Energy Environ. Sci.* **10**, 604–613 (2017).
- Christians, J. A. et al. Tailored interfaces of unencapsulated perovskite solar cells for $>1,000$ hour operational stability. *Nat. Energy* **3**, 68–74 (2018).
- Akkerman, Q. A., Rainò, G., Kovalenko, M. V. & Manna, L. Genesis, challenges and opportunities for colloidal lead halide perovskite nanocrystals. *Nat. Mater.* **17**, 394–405 (2018).
- Li, M. et al. Low threshold and efficient multiple exciton generation in halide perovskite nanocrystals. *Nat. Commun.* **9**, 4197 (2018).
- Pan, J. et al. Bidentate ligand-passivated CsPbI_3 perovskite nanocrystals for stable near-unity photoluminescence quantum yield and efficient red light-emitting diodes. *J. Am. Chem. Soc.* **140**, 562–565 (2018).
- Zheng, W. et al. Near-infrared-triggered photon upconversion tuning in all-inorganic cesium lead halide perovskite quantum dots. *Nat. Commun.* **9**, 3462 (2018).
- Zhou, D. et al. Cerium and ytterbium codoped halide perovskite quantum dots: a novel and efficient downconverter for improving the performance of silicon solar cells. *Adv. Mater.* **29**, 1704149 (2017).
- Shockley, W. & Queisser, H. J. Detailed balance limit of efficiency of p-n junction solar cells. *J. Appl. Phys.* **32**, 510–519 (1961).
- Swarnkar, A. et al. Quantum dot-induced phase stabilization of $\alpha\text{-CsPbI}_3$ perovskite for high-efficiency photovoltaics. *Science* **354**, 92–95 (2016).
- Xue, J. et al. Surface ligand management for stable FAPbI_3 perovskite quantum dot solar cells. *Joule* **2**, 1866–1878 (2018).
- Yuan, J. et al. Band-aligned polymeric hole transport materials for extremely low energy loss $\alpha\text{-CsPbI}_3$ perovskite nanocrystal solar cells. *Joule* **2**, 2450–2463 (2018).
- Sanehira, E. M. et al. Enhanced mobility CsPbI_3 quantum dot arrays for record-efficiency, high-voltage photovoltaic cells. *Sci. Adv.* **3**, eaao4204 (2017).
- Wheeler, L. M. et al. Targeted ligand-exchange chemistry on cesium lead halide perovskite quantum dots for high-efficiency photovoltaics. *J. Am. Chem. Soc.* **140**, 10504–10513 (2018).
- Lin, J. et al. Thermochromic halide perovskite solar cells. *Nat. Mater.* **17**, 261–267 (2018).

32. Kubicki, D. J. et al. Cation dynamics in mixed-cation $(MA)_x(FA)_{1-x}PbI_3$ hybrid perovskites from solid-state NMR. *J. Am. Chem. Soc.* **139**, 10055–10061 (2017).
33. Zhu, H. et al. Screening in crystalline liquids protects energetic carriers in hybrid perovskites. *Science* **353**, 1409–1413 (2016).
34. Protesescu, L. et al. Dismantling the ‘red wall’ of colloidal perovskites: highly luminescent formamidinium and formamidinium–cesium lead iodide nanocrystals. *ACS Nano* **11**, 3119–3134 (2017).
35. Lignos, I. et al. Exploration of near-infrared-emissive colloidal multinary lead halide perovskite nanocrystals using an automated microfluidic platform. *ACS Nano* **12**, 5504–5517 (2018).
36. Hazarika, A. et al. Perovskite quantum dot photovoltaic materials beyond the reach of thin films: full-range tuning of A-site cation composition. *ACS Nano* **12**, 10327–10337 (2018).
37. Suri, M. et al. Enhanced open-circuit voltage of wide-bandgap perovskite photovoltaics by using alloyed $(FA_{1-x}Cs_x)Pb(I_{1-x}Br_x)_3$ quantum dots. *ACS Energy Lett.* **4**, 1954–1960 (2019).
38. Zhao, Q. et al. High efficiency perovskite quantum dot solar cells with charge separating heterostructure. *Nat. Commun.* **10**, 2842 (2019).
39. Meggiolaro, D. et al. Iodine chemistry determines the defect tolerance of lead-halide perovskites. *Energy Environ. Sci.* **11**, 702–713 (2018).
40. Meggiolaro, D. & De Angelis, F. First-principles modeling of defects in lead halide perovskites: best practices and open issues. *ACS Energy Lett.* **3**, 2206–2222 (2018).
41. Stolterfoht, M. et al. The impact of energy alignment and interfacial recombination on the internal and external open-circuit voltage of perovskite solar cells. *Energy Environ. Sci.* **12**, 2778–2788 (2019).
42. Boyd, C. C., Cheacharoen, R., Leijtens, T. & McGehee, M. D. Understanding degradation mechanisms and improving stability of perovskite photovoltaics. *Chem. Rev.* **119**, 3418–3451 (2019).
43. Draguta, S. et al. Rationalizing the light-induced phase separation of mixed halide organic–inorganic perovskites. *Nat. Commun.* **8**, 200 (2017).
44. Gualdrón-Reyes, A. F. et al. Controlling the phase segregation in mixed halide perovskites through nanocrystal size. *ACS Energy Lett.* **4**, 54–62 (2019).
45. Protesescu, L. et al. Nanocrystals of cesium lead halide perovskites ($CsPbX_3$, $X = Cl, Br$, and I): Novel optoelectronic materials showing bright emission with wide color gamut. *Nano Lett.* **15**, 3692–3696 (2015).
46. Grabolle, M. et al. Determination of the fluorescence quantum yield of quantum dots: suitable procedures and achievable uncertainties. *Anal. Chem.* **81**, 6285–6294 (2009).
47. Chen, P. et al. In situ growth of 2D perovskite capping layer for stable and efficient perovskite solar cells. *Adv. Funct. Mater.* **28**, 1706923 (2018).
48. Shi, D. et al. Low trap-state density and long carrier diffusion in organolead trihalide perovskite single crystals. *Science* **347**, 519–522 (2015).
49. Mizusaki, J., Arai, K. & Fueki, K. Ionic conduction of the perovskite-type halides. *Solid State Ion.* **11**, 203–211 (1983).

Acknowledgements

Financial support from the Australian Research Council Discovery Projects (ARC DPs) is appreciated. Y.B. acknowledges the support from UQ Development Fellowship and ARC DECRA Fellowship (DE190101351). We acknowledge the facilities and the scientific support from the Queensland node of the Australian National Fabrication Facility and Australian Microscopy & Microanalysis Research Facility at the Centre for Microscopy and Microanalysis, The University of Queensland. We also acknowledge the use of the facilities at the University of Wollongong Electron Microscopy Centre funded by the ARC (grant nos. LE0882813 and LE120100104). Y.D. acknowledges financial support from the ARC (grant nos. DP160102627, DP170101467 and FT180100585). All computations were undertaken on the supercomputers in National Computational Infrastructure (NCI) in Canberra, which is supported by the Australian Commonwealth Government, and Pawsey Supercomputing Centre in Perth, with funding from the Australian Government and the Government of Western Australia. P.M. is a Sêr Cymru II National Research Chair and A.A. a Sêr Cymru II Rising Star Fellow. The work at Swansea University was funded through the Sêr Cymru II (Welsh European Funding Office and European Regional Development Fund) Program ‘Sustainable Advanced Materials’. Financial support from National Natural Science Foundation of China (grant nos. 51629201 and 51825204) is also appreciated.

Author contributions

Y.B., M.H. and L.W. conceived the project. L.W. and Y.B. supervised the work. M.H. synthesized the perovskite quantum dot materials, fabricated and characterized the QD thin films and devices with the assistance of S.D. Y.B. designed the experiments for understanding the ligand-assisted cation-exchange reaction mechanism and the role of surface ligands. S.Z., N.Z., A.A. and P.M. conducted the electrical and photophysical characterization of QD devices. L.R., N.C. and Y.D. performed the STEM study and analysis. J.L. and Y.W. conducted DFT calculations. M.G., M.L. and J.-H.Y. performed the cross-sectional TEM characterization. Y.Y. conducted the ion conductivity measurements. P.C. and D.H. fabricated perovskite thin films and devices. Y.B. drafted the manuscript with help from M.H., A.A., L.R., and J.L. L.W., P.M., G.L. and H.M.-C. revised the manuscript. All the authors discussed the results and commented on the manuscript.

Competing interests

The authors declare no competing interests.

Additional information

Supplementary information is available for this paper at <https://doi.org/10.1038/s41560-019-0535-7>.

Correspondence and requests for materials should be addressed to Y.B. or L.W.

Reprints and permissions information is available at www.nature.com/reprints.

Publisher’s note Springer Nature remains neutral with regard to jurisdictional claims in published maps and institutional affiliations.

© The Author(s), under exclusive licence to Springer Nature Limited 2020

Solar Cells Reporting Summary

Nature Research wishes to improve the reproducibility of the work that we publish. This form is intended for publication with all accepted papers reporting the characterization of photovoltaic devices and provides structure for consistency and transparency in reporting. Some list items might not apply to an individual manuscript, but all fields must be completed for clarity.

For further information on Nature Research policies, including our [data availability policy](#), see [Authors & Referees](#).

► Experimental design

Please check: are the following details reported in the manuscript?

1. Dimensions

Area of the tested solar cells

Yes
 No

This information can be found in the "Solar cell testing" part of Section "Methods".

Method used to determine the device area

Yes
 No

A metal shadow mask (0.058 cm²) was used to define the active area of devices.

2. Current-voltage characterization

Current density-voltage (J-V) plots in both forward and backward direction

Yes
 No

"Solar cell testing" part of Section "Methods" and Supplementary Figure 12 and 15.

Voltage scan conditions

For instance: scan direction, speed, dwell times

Yes
 No

"Solar cell testing" part of Section "Methods".

Test environment

For instance: characterization temperature, in air or in glove box

Yes
 No

"Solar cell testing" part of Section "Methods".

Protocol for preconditioning of the device before its characterization

Yes
 No

There was no preconditioning before measurement.

Stability of the J-V characteristic

Verified with time evolution of the maximum power point or with the photocurrent at maximum power point; see ref. 7 for details.

Yes
 No

Section "Stability of Cs₁-xF_xPbI₃ QD films and devices".

3. Hysteresis or any other unusual behaviour

Description of the unusual behaviour observed during the characterization

Yes
 No

No obvious hysteresis observed, stated in Section "QD device architecture and performance".

Related experimental data

Yes
 No

Supplementary Figure 12 and 15

4. Efficiency

External quantum efficiency (EQE) or incident photons to current efficiency (IPCE)

Yes
 No

Section "QD device architecture and performance".

A comparison between the integrated response under the standard reference spectrum and the response measure under the simulator

Yes
 No

Section "QD device architecture and performance".

For tandem solar cells, the bias illumination and bias voltage used for each subcell

Yes
 No

Not tandem solar cells.

5. Calibration

Light source and reference cell or sensor used for the characterization

Yes
 No

"Solar cell testing" part of Section "Methods".

Confirmation that the reference cell was calibrated and certified

Yes
 No

"Solar cell testing" part of Section "Methods".

<p>Calculation of spectral mismatch between the reference cell and the devices under test</p> <p>6. Mask/aperture</p> <p>Size of the mask/aperture used during testing</p> <p>Variation of the measured short-circuit current density with the mask/aperture area</p> <p>7. Performance certification</p> <p>Identity of the independent certification laboratory that confirmed the photovoltaic performance</p> <p>A copy of any certificate(s) <i>Provide in Supplementary Information</i></p> <p>8. Statistics</p> <p>Number of solar cells tested</p> <p>Statistical analysis of the device performance</p> <p>9. Long-term stability analysis</p> <p>Type of analysis, bias conditions and environmental conditions <i>For instance: illumination type, temperature, atmosphere humidity, encapsulation method, preconditioning temperature</i></p>	<input type="checkbox"/> Yes <input checked="" type="checkbox"/> No <div style="border: 1px solid black; padding: 5px; margin-top: 10px;">Calculation is not reported but we reported all needed information including our device spectrum and the model of Silicon reference cell (Newport 91150V) in "Solar cell testing" part of Section "Methods".</div> <input checked="" type="checkbox"/> Yes <input type="checkbox"/> No <div style="border: 1px solid black; padding: 5px; margin-top: 10px;">"Solar cell testing" part of Section "Methods".</div> <input type="checkbox"/> Yes <input checked="" type="checkbox"/> No <div style="border: 1px solid black; padding: 5px; margin-top: 10px;">The short-circuit current density doesn't vary with the mask/aperture area.</div> <input checked="" type="checkbox"/> Yes <input type="checkbox"/> No <div style="border: 1px solid black; padding: 5px; margin-top: 10px;">The champion device was certified in Newport PV lab, USA.</div> <input checked="" type="checkbox"/> Yes <input type="checkbox"/> No <div style="border: 1px solid black; padding: 5px; margin-top: 10px;">The Newport certificate has been included as Supplementary Figure 13.</div> <input checked="" type="checkbox"/> Yes <input type="checkbox"/> No <div style="border: 1px solid black; padding: 5px; margin-top: 10px;">Section "QD device architecture and performance" and Figure 3.</div> <input checked="" type="checkbox"/> Yes <input type="checkbox"/> No <div style="border: 1px solid black; padding: 5px; margin-top: 10px;">Section "QD device architecture and performance".</div> <input checked="" type="checkbox"/> Yes <input type="checkbox"/> No <div style="border: 1px solid black; padding: 5px; margin-top: 10px;">Section "Stability of Cs_{1-x}FA_xPbI₃ QD films and devices".</div>
---	---